Nanoscale Advances

ROYAL SOCIETY OF CHEMISTRY

PAPER

View Article Online
View Journal | View Issue

Cite this: *Nanoscale Adv.*, 2022, **4**, 2744

Reconfigurable carrier type and photodetection of $MoTe_2$ of various thicknesses by deep ultraviolet light illumination†

Byung Min Ko,‡[a] Muhammad Farooq Khan, ‡[b] Ghulam Dastgeer,[a] Gyu Nam Han,[a] Muhammad Asghar Khan[a] and Jonghwa Eom *[a]

Tuning of the Fermi level in transition metal dichalcogenides (TMDCs) leads to devices with excellent electrical and optical properties. In this study, we controlled the Fermi level of $MoTe_2$ by deep ultraviolet (DUV) light illumination in different gaseous environments. Specifically, we investigated the reconfigurable carrier type of an intrinsic p-$MoTe_2$ flake that gradually transformed into n-$MoTe_2$ after illumination with DUV light for 30, 60, 90, 120, 160, 250, 500, 900, and 1200 s in a nitrogen (N_2) gas environment. Subsequently, we illuminated this n-$MoTe_2$ sample with DUV light in oxygen (O_2) gas and reversed its carrier polarity toward p-$MoTe_2$. However, using this doping scheme to reveal the effect of DUV light on various layers (3–30 nm) of $MoTe_2$ is challenging. The DUV + N_2 treatment significantly altered the polarity of $MoTe_2$ of different thicknesses from p-type to n-type under the DUV + N_2 treatment, but the DUV + O_2 treatment did not completely alter the polarity of thicker n-$MoTe_2$ flakes to p-type. In addition, we investigated the photoresponse of $MoTe_2$ after DUV light treatment in N_2 and O_2 gas environments. From the time-resolved photoresponsivity at different polarity states of $MoTe_2$, we have shown that the response time of the DUV + O_2 treated p-$MoTe_2$ is faster than that of the pristine and doped n-$MoTe_2$ films. These carrier polarity modulations and photoresponse paves the way for wider applications of $MoTe_2$ in optoelectronic devices.

Received 22nd December 2021
Accepted 9th May 2022

DOI: 10.1039/d1na00881a

rsc.li/nanoscale-advances

Introduction

Recently, two-dimensional (2D) nanomaterials have gained significant attention because of their unique optical and electrical properties.[1–3] Graphene has been the focus of modern research in the past few years because of its high intrinsic electron mobility of 200 000 $cm^2\ V\ s^{-1}$ and high thermal conductivity of approximately 4400 to 5780 $W\ m\ K^{-1}$ at room temperature.[4,5] In addition, the transmittance of light was found to be 97.7% at 550 nm owing to the small thickness of a single layer.[6] However, the absence of the bandgap in graphene initiates the search for other 2D bandgap materials, which is necessary for switching device applications. Transition metal dichalcogenides (TMDCs) have a significant bandgap range of approximately 1.0 to 2.5 eV, which facilitates fabrication of atomically thin p–n diodes such as $MoTe_2/MoS_2$, WSe_2/MoS_2 and black phosphorus/IGZO.[7–9] The Fermi level of TMDCs is near the center between conduction and valence bands,[10] but most TMDCs used in experiments are naturally n-type or p-type doped due to intrinsic structural defects and interface impurities.[11,12]

Controlled modulation of the Fermi level in the bandgap of TMDCs has been exploited in various reports for device applications.[13,14] While most of the well-known TMDCs such as WS_2, MoS_2, $MoSe_2$, $ReSe_2$, and ReS_2 are observed to be n-type semiconductors, $MoTe_2$ is p-type when thin, and shows ambipolar and n-type properties in thicker forms.[15–19] In addition, $MoTe_2$ has shown great potential in applications, such as chemical sensors, memristors, and photodetectors.[20–22] The thicker hexagonal structure of $MoTe_2$ has a bandgap of 0.88 eV, whereas its mono-layer exhibits a direct bandgap of almost 1.1 eV.[23,24] The narrow bandgap also enables a huge tunneling current and a high on-off ratio of $MoTe_2$ FETs. The pinning of the Fermi level at the $MoTe_2$-metal interface is not as strong as that of sulfur-terminated TMDCs.[25] Thus, the weak pinning and small bandgap of $MoTe_2$ make the Fermi level modulation feasible and carrier polarity controllable by various techniques. The doping treatment of $MoTe_2$ has been accomplished by electrostatic gating, chemical doping, and work function engineering with different metal electrodes; however, the doping effect was weak and too volatile for electronic devices.[26–28] Designing a constructive approach that provides non-volatility and

[a]*Department of Physics & Astronomy and Graphene Research Institute, Sejong University, Seoul 05006, Korea. E-mail: eom@sejong.ac.kr*

[b]*Department of Electrical Engineering, Sejong University, 209 Neungdong-ro, Gwangjin-gu, Seoul 05006, Korea*

† Electronic supplementary information (ESI) available. See https://doi.org/10.1039/d1na00881a

‡ These authors contributed equally.

reversibility of charge carrier polarity in 2D TMDC materials is indispensable. Therefore, $MoTe_2$ with layers of different thicknesses is a promising candidate for overcoming the above-mentioned challenges. However, there is still ambiguity in the doping effect and carrier-type inversion of $MoTe_2$ layers with different thicknesses when exposed to deep ultraviolet (DUV) light in various gaseous environments.

In this study, we fabricated a $MoTe_2$ field-effect transistor (FET) on a SiO_2 substrate using the mechanical exfoliation technique. We exposed $MoTe_2$ thin-film FETs under deep ultraviolet (DUV) light for different illumination times in the presence of different gases (N_2 or O_2), which resulted in a non-volatile doping effect and inversion of charge carrier polarity in $MoTe_2$ FETs. In addition, we investigated the photodetection of DUV light after a variety of doping treatments (pristine p-$MoTe_2$, DUV + N_2 treatment, and DUV + O_2 treatment).

Fabrication

We fabricated a $MoTe_2$ FET on a SiO_2 substrate (Fig. 1a) to elucidate the carrier polarity modification. Bulk $MoTe_2$ was first put on tape and then exfoliated to make the $MoTe_2$ thin films.[29] Then, the tape was pressed on top of polydimethylsiloxane (PDMS). Subsequently, PDMS was stamped on the desired area on the Si/SiO_2 substrates.[30] A $MoTe_2$ thin film was produced as confirmed using optical microscopy. Then, conventional e-beam lithography was employed to make Cr/Au (5 nm/60 nm) electrical contacts, which were annealed at 100 °C for 1.5 h to improve the ohmic properties.[30–32] The optical microscope images of the final device are shown in Fig. 1a. Meanwhile, the thickness of the flakes was investigated using atomic force microscopy (AFM). Fig. 1b and c show the AFM images of the film and the thickness of the exfoliated $MoTe_2$ film was found to be approximately 6.5 nm.[15,33] Then, the crystal properties of $MoTe_2$ were examined by Raman spectroscopy[15] as shown in Fig. 1d.

Furthermore, the DUV doping treatments were performed in N_2 and O_2 gas environments at a pressure of 0.8 bar. The average intensity of the DUV light was 11 mW cm^{-2}, which was measured at a wavelength of 220 nm.

Results and discussion

Transition from intrinsic p-type $MoTe_2$ to n-type $MoTe_2$

Raman spectroscopy was performed to examine the crystal bonding properties and estimate the thickness of the pristine $MoTe_2$ flakes. Fig. 1d shows the Raman spectrum of $MoTe_2$ obtained using a Renishaw microspectrometer with a laser wavelength of 514 nm and an optical intensity of 1 mW cm^{-2}. Three vibrational modes were observed, namely, A_g^1, E_1^{2g} and B_1^{2g} at approximately 173.8 cm^{-1}, 236.2 cm^{-1}, and 291.1 cm^{-1}, respectively. These results reveal five layers of $MoTe_2$, which is almost consistent with previous reports.[34,35]

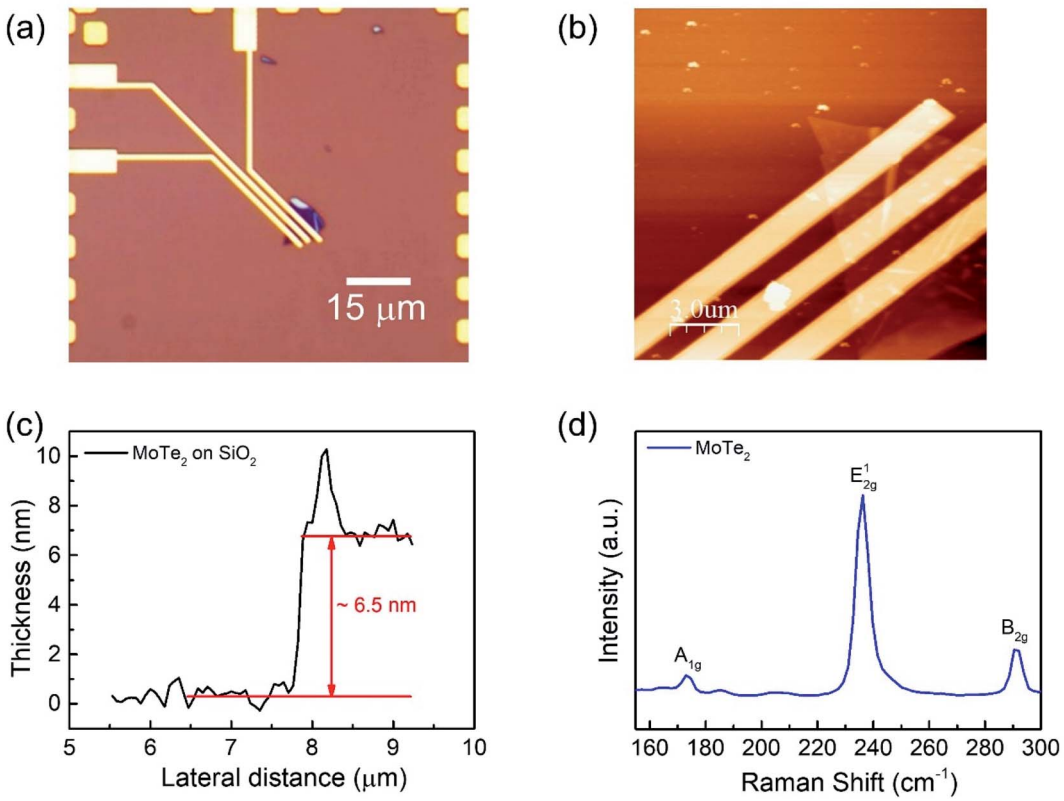

Fig. 1 (a) Optical microscope image of the $MoTe_2$ device. (b) Atomic force microscopy (AFM) image of the $MoTe_2$ device. (c) The thickness profile of the $MoTe_2$ thin film by AFM. (d) The Raman spectroscopy image of the $MoTe_2$ film under ambient conditions.

Furthermore, we investigated the intrinsic nature of the charge carriers of the $MoTe_2$ flakes by measuring the transfer curves (I_{ds} *vs.* V_g) at a fixed source–drain bias voltage $V_{ds} = 1$ V. After sweeping the gate voltage from −60 to 60 V, a threshold current (I_{ds}) was observed in the negative gate voltage regime, confirming the p-type nature of the pristine $MoTe_2$ flake, as shown in Fig. 2a. Subsequently, we treated the pristine p-$MoTe_2$ with DUV light in a N_2 environment (DUV + N_2) for 1200 s to obtain n-$MoTe_2$. The change in the charge carrier type was confirmed by using the I_{ds}–V_g transfer curves, as shown in Fig. 2b. The DUV exposure time was varied from 0 to 1200 s, with a time interval of 30 s. The DUV + N_2 treatment gave rise to n-type doping in $MoTe_2$. The Fermi level of the intrinsic p-type $MoTe_2$ was near the valence band, but after the DUV + N_2 treatment, the Fermi level shifted near the conduction band. This Fermi level shift is responsible for the change in the nature of the $MoTe_2$ flakes from p- to n-type. To verify the doping mechanism more precisely, the mobility of electrons/holes of intrinsic p-$MoTe_2$ and n-$MoTe_2$ (after DUV + N_2 treatment) sheets was extracted from the transfer curves using the following equation:

$$\mu = \frac{L}{WC_g V_{ds}} \frac{dI_{ds}}{dV_g} \quad (1)$$

Here, L (W) is the length (width) of the active channel area of $MoTe_2$ nano-sheets, $C_g = 11.5$ nF cm^{-2}, is the gate capacitance,[36] and V_{ds} (I_{ds}) is the source–drain voltage (current). In this work, we used a $MoTe_2$ device with $L = 1$ μm and $W = 5.6$ μm, whereas the source–drain voltage was fixed at 1 V. Notably, the hole mobility gradually decreased from 11 cm^2 V^{-1} s^{-1} to almost zero, while the electron mobility began to increase from 0.1 to 40 cm^2 V^{-1} s^{-1} as the $MoTe_2$ flakes underwent DUV + N_2 treatment, as shown in Fig. 2c. This treatment made the doping of intrinsic p-$MoTe_2$ and changed the carrier type from p-type to n-type after undergoing ambipolar behavior. The sample finally transformed into n-$MoTe_2$ as the exposure time reached 1200 s.

Moreover, the charge carrier density of holes in p-type $MoTe_2$ and electrons in DUV + N_2 treated $MoTe_2$ sheets was calculated using the relation:[37,38]

$$n = q^{-1}C_g|V_{th} - V_g| \quad (2)$$

where $q = 1.6 \times 10^{-19}$ C is the charge of the electron, $C_g = 11.5$ nF cm^{-2} is the gate capacitance, V_{th} is the threshold voltage observed in the transfer curve, and V_g is the applied gate voltage (±40 V). Therefore, we can determine the carrier density of $MoTe_2$ according to the change in the threshold voltage. When the DUV + N_2 exposure time was zero, the electron density was significantly small (3.7×10^{11} cm^{-2}) compared to the hole density (7.4×10^{11} cm^{-2}), and the dominant carrier type was reversed over time. Therefore, the N_2 gas under DUV light removes oxygen on the surface of $MoTe_2$, which alters its intrinsic p-type nature to n-type $MoTe_2$, as shown in Fig. 2d.

Transition from n-type $MoTe_2$ to p-type $MoTe_2$

Interestingly, the n-$MoTe_2$ flake, which was treated with DUV + N_2 for 1200 s, could be reconfigured to p-$MoTe_2$ by DUV + O_2

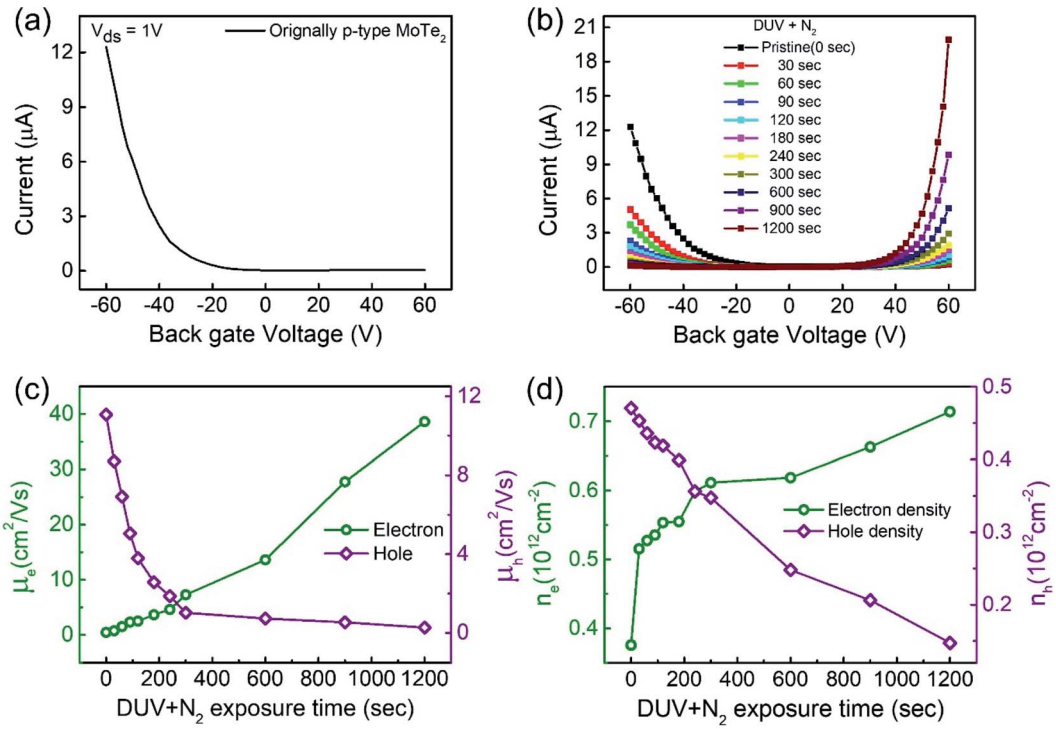

Fig. 2 (a) Transfer curve (I_{ds}–V_g) of the intrinsic p-$MoTe_2$ device. (b) The transfer curves at different DUV + N_2 treatment times. (c) Electron and hole mobility at different DUV + N_2 treatment times. (d) The charge carrier density of electrons and holes of the $MoTe_2$ flake for various DUV + N_2 treatment times.

treatment. As mentioned previously, the source–drain voltage was fixed at $V_{ds} = 1$ V, and the back-gate voltage was applied to the substrate to check the I_{ds}–V_g transfer curve from 60 V to −60 V. Fig. 3a shows the transfer curve of n-$MoTe_2$ treated with DUV + N_2 for 1200 s. Then, the transfer curves were measured as we increased the treatment time of DUV + O_2, as shown in Fig. 3b. The mobility of the electrons (holes) in the n-$MoTe_2$ sheets was estimated to be 0.25 $cm^2\ V^{-1}\ s^{-1}$ (3.8 $cm^2\ V^{-1}\ s^{-1}$) after the DUV + O_2 treatment, as shown in Fig. 3c. As the exposure time of the DUV + O_2 treatment increased from 0 to 1200 s, the mobility of electrons decreased, while the mobility of holes increased. Similarly, the carrier density of the holes (electrons) at a fixed gate voltage of ±40 V increased (decreased) with increasing exposure time, as shown in Fig. 3d. Initially, the carrier density increased abruptly but started to saturate with time after 200 s. The increase in the hole density indicates that the nature of n-type $MoTe_2$ shifted back to that of p-type $MoTe_2$ after the DUV + O_2 treatment. This reverse doping could be ascribed to the oxygen donor molecules under DUV light, and the shift of the $MoTe_2$ Fermi level near the valence band. In case of transition from pristine p-$MoTe_2$ to n-$MoTe_2$, the current and mobility values are saturated after 1200 s DUV + N_2 treatment as shown in Fig. S2a and S2b (see the ESI†). On the other hand, when n-type doped $MoTe_2$ (self-made) is converted to p-$MoTe_2$ by DUV + O_2 treatment, the current and mobility values reach the maximum values, but after 1200 s they slightly start to degrade due to weak oxidation of $MoTe_2$ under DUV + O_2 treatment (see Fig. S1c and S1d†).

In addition, we investigated several intrinsic p-$MoTe_2$ devices with different flake thickness values under DUV light in N_2 and O_2 environments. AFM images and thickness profiles of the devices are shown in Fig. S2.† As shown in Fig. 4a, we measured the I_{ds}–V_g curves of intrinsic $MoTe_2$ devices with different thicknesses (3.1, 5.9, 14, and 30 nm). However, we found that the thin flake devices showed only p-type behavior, whereas the thicker flakes showed ambipolar or n-type characteristics. After the DUV + N_2 treatment, all devices were then completely configured into n-type, as shown in Fig. 4b. Subsequently, we exposed the n-$MoTe_2$ devices to DUV + O_2 treatment, which altered all the n-type devices to p-type. Interestingly, only the thin devices completely changed their polarities. The thicker devices did not completely change back to p-type but showed ambipolar behavior, as shown in Fig. 4c. The DUV + O_2 treatment did not fully dope the thick flakes. Furthermore, the mobilities of electrons and holes for all devices (pristine, after DUV + N_2, and DUV + O_2 treatments) were estimated, as shown in Fig. 4d and e. While the 3.1 nm-thick $MoTe_2$ flake was p-type in the pristine state, the 30 nm-thick $MoTe_2$ flake was n-type in the pristine state. We found that the DUV treatments were more efficient for thinner $MoTe_2$ flakes.

Photodetector measurements

The key factors in photodetection are current photo-generation and photoresponsivity, which play promising roles in optical devices. Therefore, the time-resolved photoresponse of the fabricated FETs was examined under a DUV lamp ($\lambda = 220$ nm, $P = 11$ mW cm^{-2}) in a vacuum box. The newly fabricated device

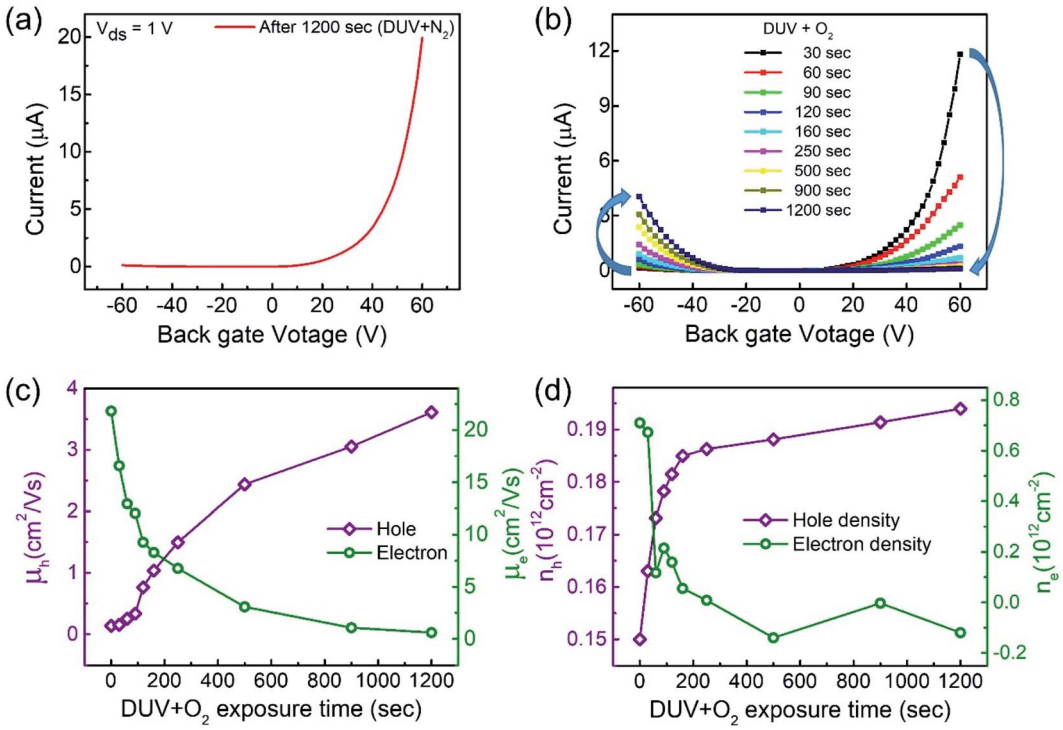

Fig. 3 (a) Transfer curve of the $MoTe_2$ device after DUV + N_2 doping for 1200 s. (b) Transfer curves after DUV + O_2 treatments for various times. (c) Electron and hole mobility for various DUV + O_2 treatment times. (d) Charge carrier density of electrons and holes of the $MoTe_2$ flake for various DUV + O_2 treatment times.

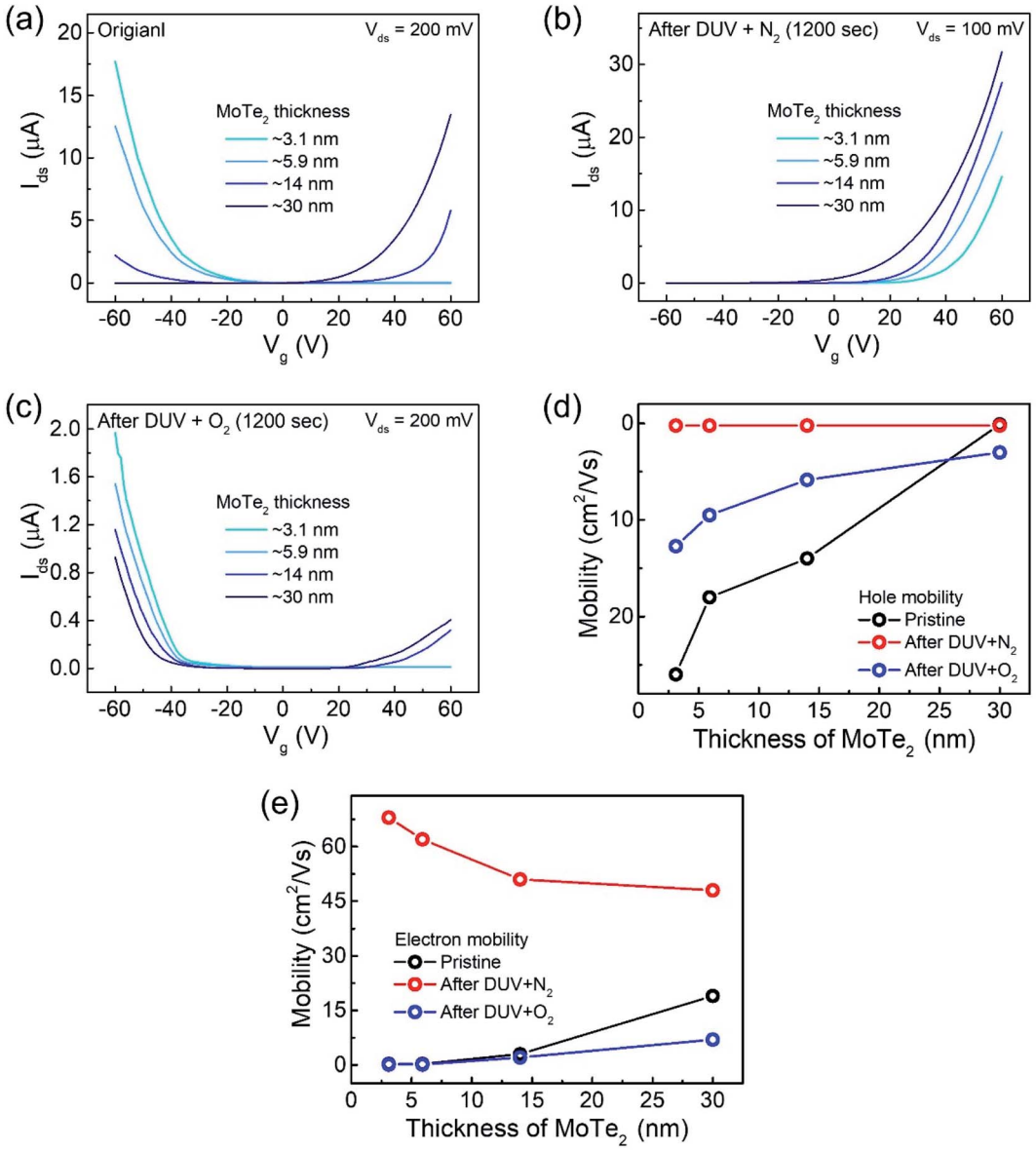

Fig. 4 Transfer curves of (a) pristine p-$MoTe_2$ flakes. (b) DUV + N_2 treated $MoTe_2$ flakes. (c) DUV + O_2 treated $MoTe_2$ flakes. (d) Hole mobility of all devices having different thicknesses of $MoTe_2$. (e) Electron mobility of all devices with different thicknesses of $MoTe_2$.

was first imaged as shown in Fig. 5a. For comparison, the response of the pristine p-$MoTe_2$, n-$MoTe_2$ after DUV + N_2 treatment, and p-$MoTe_2$ after DUV + O_2 treatment under DUV light irradiation was observed in a vacuum at $V_g = 0$ V and $V_{ds} =$ 0.5 V. When the DUV light on the pristine p-$MoTe_2$ photodetector was switched ON (for 60 s), a photocurrent was generated owing to electron–hole pair generation. Then, the photocurrent quickly dropped toward its initial state when the DUV light was switched OFF (for 60 s), as shown in Fig. 5b. The photoresponse of the pristine $MoTe_2$ device is shown in Fig. 5b.

Meanwhile, the self-made n-$MoTe_2$ photodetector after DUV + N_2 doping showed a faster response with higher photocurrent values, as shown in Fig. 5c. This increase in the photocurrent is likely due to the large electron density caused by DUV + N_2 doping, which facilitates the charge carrier transport after the generation of electron–hole pairs by DUV light. Furthermore, for the self-made p-$MoTe_2$ device after DUV + O_2 doping, the photoresponse is faster but the photocurrent magnitude is reduced, as shown in Fig. 5d. The reduced current is attributed to the oxygen trap states formed by DUV + O_2. However, the sharp rise and decay of the n-$MoTe_2$ and p-$MoTe_2$ photodetectors (Fig. 5c and d) are expected to occur because of the additional energy states in $MoTe_2$ (n- and p-type) with N_2 and O_2 treatment under DUV light. When the DUV light is turned ON, an abrupt rise in the photocurrent is produced due to electron–hole pair generation, but electrons are quickly captured in trapping states of the defects and the current quickly falls down to a saturation level.

To elucidate the photoresponse in detail, we calculated the photoresponsivity of each device (Fig. 6a). The responsivities of

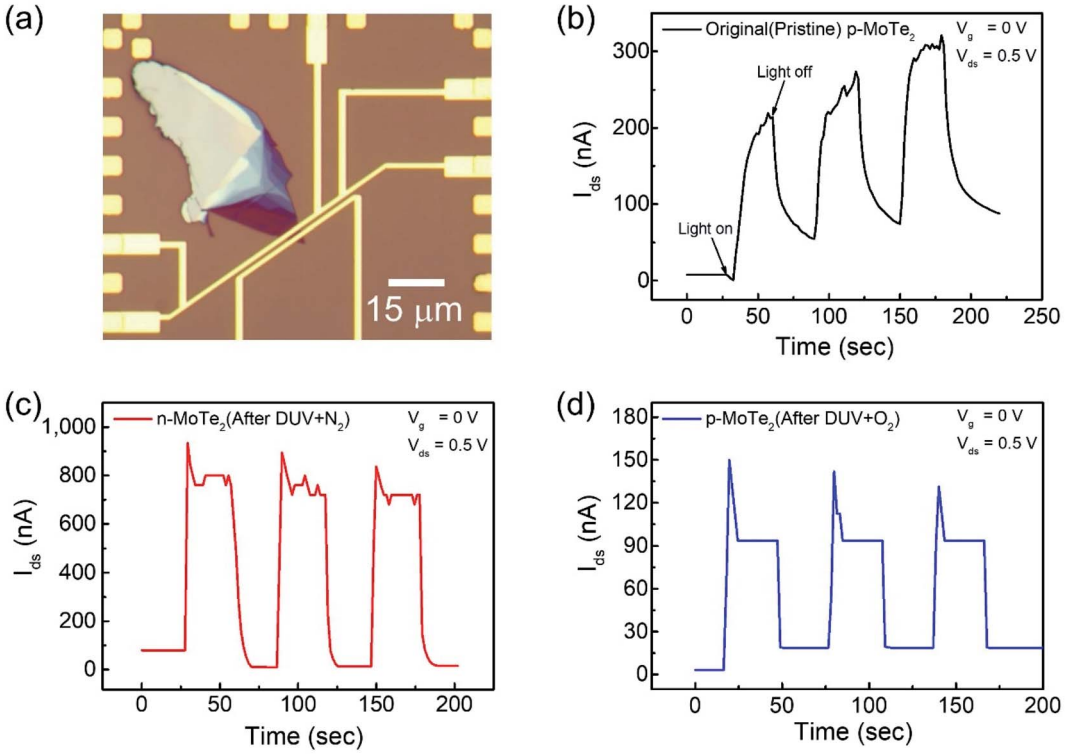

Fig. 5 (a) Optical microscope image of the pristine p-$MoTe_2$ device. Photoresponse of (b) pristine p-$MoTe_2$, (c) after 1200 s DUV + N_2 treatment and (d) after 1200 s DUV + O_2 treatment.

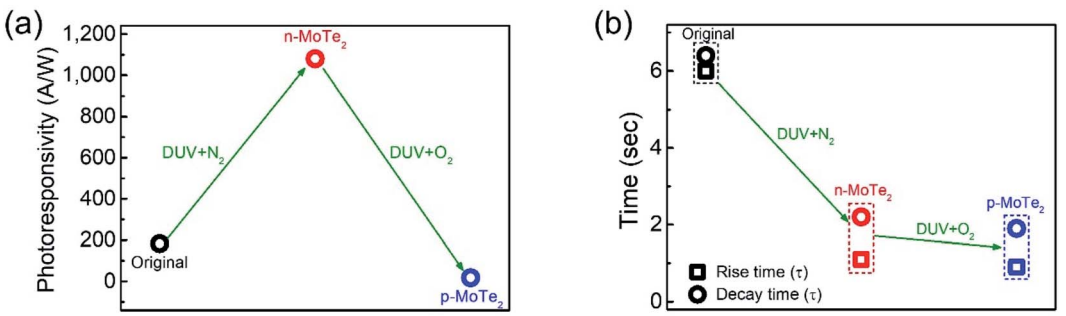

Fig. 6 (a) Photoresponsivity of pristine p-$MoTe_2$, DUV + N_2 treated and DUV + O_2 treated devices. (b) Response time (rise & decay) of $MoTe_2$ photodetectors of each type. The rectangular shape represents the rise time constant and circle shape represents the decay time constant.

pristine $MoTe_2$, DUV + N_2 doped $MoTe_2$ (n-$MoTe_2$), and DUV + O_2 doped $MoTe_2$ (p-$MoTe_2$) were found to be approximately 183, 1080, and 18 A/W, respectively. This trend is expected because the DUV + O_2 treated p-$MoTe_2$ device exhibited low photocurrent generation (approximately 12 nA) compared to pristine p-$MoTe_2$ (110 nA) and DUV + N_2 doped devices (713 nA), as shown in Fig. S3.† The lower photocurrent in the DUV + O_2 treated devices can be ascribed to the quick recombination of photogenerated charges in defect states of p-type $MoTe_2$.

The response times of the pristine $MoTe_2$, DUV + N_2 doped n-$MoTe_2$, and DUV + O_2 doped p-$MoTe_2$ devices were also extracted after fitting the following equations:[39,40]

$$I_t = I_{dark} + A(1 - e^{-t/\lambda_1}) \text{ and } I_t = I_{dark} + Be^{-t/\lambda_2} \quad (3)$$

here, λ_1 is the rise time constant, λ_2 is the decay time constant, and A and B are the scaling constants used as fitting parameters. The rise/decay times of pristine p-$MoTe_2$ and treated n-$MoTe_2$ and p-$MoTe_2$ photodetectors were estimated as 6/6.4, 1.1/2.2 and 0.9/1.9 s, respectively, as shown in Fig. 6b. The decay and rise times were reduced as the pristine p-$MoTe_2$ was treated with DUV + N_2 and DUV + O_2, which are related to the additional defects/energy states in the mid-gap of $MoTe_2$ after DUV irradiation in N_2 and O_2 environments.

Conclusion

In summary, FETs were fabricated using pristine p-$MoTe_2$, n-$MoTe_2$ (after DUV + N_2 treatment), and p-$MoTe_2$ (after DUV + O_2

treatment). The pristine p-$MoTe_2$ gradually changed to n-$MoTe_2$ after DUV + N_2 treatment. Subsequently, the treated n-$MoTe_2$ was reconfigured to p-$MoTe_2$ by DUV + O_2 treatment. We estimated that the field-effect mobility and charge carrier density of electrons/holes significantly changed under the DUV + N_2/O_2 treatments. In addition, we investigated each type of the $MoTe_2$ photodetector at $V_g = 0$ V and found that the photocurrent of n-$MoTe_2$ was higher than that of intrinsic p-$MoTe_2$ and treated p-$MoTe_2$. The DUV + O_2 treated p-$MoTe_2$ devices exhibited slightly poor performance owing to the O_2 based electron trapping states in $MoTe_2$. Interestingly, we found that the polarity of thin $MoTe_2$ flakes could be easily changed from p-type to n-type and then from n-type to p-type, whereas the thicker $MoTe_2$ flakes could easily transform into an n-type material after DUV + N_2 treatment; however, their polarities were not entirely transformed from n-type to p-type after DUV + O_2 treatment. Moreover, we found that the response time of DUV + O_2 treated p-$MoTe_2$ is faster than that of intrinsic p-$MoTe_2$ and DUV + N_2 treated n-$MoTe_2$, which is attributed to the additional trapping/oxide states in the DUV + O_2 treated p-$MoTe_2$ flake. We believe that such a reversibility of carrier polarity by DUV + N_2/O_2 treatment can be utilized for the next generation of optoelectronic devices.

Conflicts of interest

The authors declare no competing financial interests.

Acknowledgements

This work was supported by grants No. 2021R1A4A1031900, the Basic Science Research Program (2019R1F1A1057697), and the Global Research and Development Center Program (2018K1A4A3A01064272) through a National Research Foundation of Korea (NRF) grant funded by the Korean government (Ministry of Education and the Ministry of Science and ICT).

References

1 Y. Yang, Z. Liu, K. Shu, L. Li and J. Li, *Adv. Mater. Interfaces*, 2021, 2100164.
2 X. Zhai, X. Xu, J. Peng, F. Jing, Q. Zhang, H. Liu and Z. Hu, *ACS Appl. Mater. Interfaces*, 2020, **12**, 24093–24101.
3 S. Rehman, H. Kim, M. F. Khan, J.-H. Hur, J. Eom and D.-k. Kim, *J. Alloys Compd.*, 2021, **855**, 157310.
4 K. I. Bolotin, K. J. Sikes, Z. Jiang, M. Klima, G. Fudenberg, J. Hone, P. Kim and H. L. Stormer, *Solid State Commun.*, 2008, **146**, 351–355.
5 A. A. Balandin, S. Ghosh, W. Bao, I. Calizo, D. Teweldebrhan, F. Miao and C. N. Lau, *Nano Lett.*, 2008, **8**, 902–907.
6 S.-E. Zhu, S. Yuan and G. C. A. M. Janssen, *Europhys. Lett.*, 2014, **108**, 17007.
7 A. Pezeshki, S. H. H. Shokouh, T. Nazari, K. Oh and S. Im, *Adv. Mater.*, 2016, **28**, 3216–3222.
8 R. Cheng, D. Li, H. Zhou, C. Wang, A. Yin, S. Jiang, Y. Liu, Y. Chen, Y. Huang and X. Duan, *Nano Lett.*, 2014, **14**, 5590–5597.
9 G. Dastgeer, M. F. Khan, J. Cha, A. M. Afzal, K. H. Min, B. M. Ko, H. Liu, S. Hong and J. Eom, *ACS Appl. Mater. Interfaces*, 2019, **11**, 10959–10966.
10 C. Kittel, *Introduction to Solid State Physics*, Wiley, Sussex, Eng., United Kingdom, Fifth edition, 1976.
11 D. Rhodes, S. H. Chae, R. Ribeiro-Palau and J. Hone, *Nat. Mater.*, 2019, **18**, 541–549.
12 M. F. Khan, F. Ahmed, S. Rehman, I. Akhtar, M. A. Rehman, P. A. Shinde, K. Khan, D.-k. Kim, J. Eom and H. Lipsanen, *Nanoscale*, 2020, **12**, 21280–21290.
13 D.-H. Kang, J. Shim, S. K. Jang, J. Jeon, M. H. Jeon, G. Y. Yeom, W.-S. Jung, Y. H. Jang, S. Lee and J.-H. Park, *ACS Nano*, 2015, **9**, 1099–1107.
14 S. Zhang, H. M. Hill, K. Moudgil, C. A. Richter, A. R. Hight Walker, S. Barlow, S. R. Marder, C. A. Hacker and S. J. Pookpanratana, *Adv. Mater.*, 2018, **30**, 1802991.
15 C. Ruppert, O. B. Aslan and T. F. Heinz, *Nano Lett.*, 2014, **14**, 6231–6236.
16 A. Eftekhari, *J. Mater. Chem. A*, 2017, **5**, 18299–18325.
17 O. Lopez-Sanchez, D. Lembke, M. Kayci, A. Radenovic and A. Kis, *Nat. Nanotechnol.*, 2013, **8**, 497–501.
18 M. F. Khan, S. Rehman, I. Akhtar, S. Aftab, H. M. S. Ajmal, W. Khan, D.-k. Kim and J. Eom, *2D Materials*, 2019, **7**, 015010.
19 E. Zhang, Y. Jin, X. Yuan, W. Wang, C. Zhang, L. Tang, S. Liu, P. Zhou, W. Hu and F. Xiu, *Adv. Funct. Mater.*, 2015, **25**, 4076–4082.
20 Z. Feng, Y. Xie, J. Chen, Y. Yu, S. Zheng, R. Zhang, Q. Li, X. Chen, C. Sun and H. Zhang, *2D Materials*, 2017, **4**, 025018.
21 L. Sun, M. Ding, J. Li, L. Yang, X. Lou, Z. Xie, W. Zhang and H. Chang, *Appl. Surf. Sci.*, 2019, **496**, 143687.
22 H. Huang, J. Wang, W. Hu, L. Liao, P. Wang, X. Wang, F. Gong, Y. Chen, G. Wu and W. Luo, *Nanotechnology*, 2016, **27**, 445201.
23 D. H. Keum, S. Cho, J. H. Kim, D.-H. Choe, H.-J. Sung, M. Kan, H. Kang, J.-Y. Hwang, S. W. Kim and H. Yang, *Nat. Phys.*, 2015, **11**, 482–486.
24 J. S. Cho, H. S. Ju, J.-K. Lee and Y. C. Kang, *Nanoscale*, 2017, **9**, 1942–1950.
25 C. Kim, I. Moon, D. Lee, M. S. Choi, F. Ahmed, S. Nam, Y. Cho, H.-J. Shin, S. Park and W. J. Yoo, *ACS Nano*, 2017, **11**, 1588–1596.
26 S. Larentis, B. Fallahazad, H. C. Movva, K. Kim, A. Rai, T. Taniguchi, K. Watanabe, S. K. Banerjee and E. Tutuc, *ACS Nano*, 2017, **11**, 4832–4839.
27 W. Luo, M. Zhu, G. Peng, X. Zheng, F. Miao, S. Bai, X. A. Zhang and S. Qin, *Adv. Funct. Mater.*, 2018, **28**, 1704539.
28 A. Pezeshki, S. H. Hosseini Shokouh, P. J. Jeon, I. Shackery, J. S. Kim, I.-K. Oh, S. C. Jun, H. Kim and S. Im, *ACS Nano*, 2016, **10**, 1118–1125.
29 K. S. Novoselov, *Angew. Chem., Int. Ed.*, 2011, **50**, 6986–7002.
30 R. Yang, X. Zheng, Z. Wang, C. J. Miller and P. X. L. Feng, *J. Vac. Sci. Technol., B: Nanotechnol. Microelectron.: Mater., Process., Meas., Phenom.*, 2014, **32**, 061203.
31 J. Lin, S. T. Pantelides and W. Zhou, *ACS Nano*, 2015, **9**, 5189–5197.

32 D. Qi, Q. Wang, C. Han, J. Jiang, Y. Zheng, W. Chen, W. Zhang and A. T. S. Wee, *2D Materials*, 2017, **4**, 045016.
33 I. G. Lezama, A. Arora, A. Ubaldini, C. Barreteau, E. Giannini, M. Potemski and A. F. Morpurgo, *Nano Lett.*, 2015, **15**, 2336–2342.
34 M. Grzeszczyk, K. Gołasa, M. Zinkiewicz, K. Nogajewski, M. R. Molas, M. Potemski, A. Wysmołek and A. Babiński, *2D Materials*, 2016, **3**, 025010.
35 M. Yamamoto, S. T. Wang, M. Ni, Y.-F. Lin, S.-L. Li, S. Aikawa, W.-B. Jian, K. Ueno, K. Wakabayashi and K. Tsukagoshi, *ACS Nano*, 2014, **8**, 3895–3903.
36 M. W. Iqbal, M. Z. Iqbal, M. F. Khan, M. A. Shehzad, Y. Seo, J. H. Park, C. Hwang and J. Eom, *Sci. Rep.*, 2015, **5**, 10699.
37 Y.-H. Lee, L. Yu, H. Wang, W. Fang, X. Ling, Y. Shi, C.-T. Lin, J.-K. Huang, M.-T. Chang, C.-S. Chang, M. Dresselhaus, T. Palacios, L.-J. Li and J. Kong, *Nano Lett.*, 2013, **13**, 1852–1857.
38 J. D. Lin, C. Han, F. Wang, R. Wang, D. Xiang, S. Qin, X.-A. Zhang, L. Wang, H. Zhang, A. T. S. Wee and W. Chen, *ACS Nano*, 2014, **8**, 5323–5329.
39 B. Chitara, S. B. Krupanidhi and C. N. R. Rao, *Appl. Phys. Lett.*, 2011, **99**, 113114.
40 Y. Miyamoto, D. Yoshikawa, K. Takei, T. Arie and S. Akita, *Jpn. J. Appl. Phys.*, 2018, **57**, 06HB01.